






Direct observation of large-area strain propagation on free-standing nanomembranes

Yuri Bernardes ¹, Lucas A. B. Marçal ^{2,3}, Barbara L. T. Rosa,¹ Ailton Garcia, Jr. ^{4,5}, Christoph Deneke ⁵,
Tobias U. Schüllli,⁶ Marie-Ingrid Richard,^{6,7} and Angelo Malachias ^{1,*}

¹*Departamento de Física, Universidade Federal de Minas Gerais, Avenida Antonio Carlos 6627, 31270-901, Belo Horizonte, Brazil*

²*Synchrotron Radiation Research Division and NanoLund, Lund University, Box 118, S-221 00 Lund, Sweden*

³*MAX IV Laboratory, Lund University, 22100 Lund, Sweden*

⁴*Laboratório Nacional de Nanotecnologia, Centro Nacional de Pesquisa em Energia e Materiais, 13083-100 Campinas, Brazil*

⁵*Instituto de Física “Gleb Wataghin,” Universidade Estadual de Campinas, 13083-859 Campinas, Brazil*

⁶*ESRF – The European Synchrotron, 71 Avenue des Martyrs, 38000 Grenoble, France*

⁷*Université Grenoble Alpes, CEA Grenoble, IRIG, MEM, NRS, 17 rue des Martyrs, 38000 Grenoble, France*



(Received 4 October 2022; revised 8 December 2022; accepted 10 January 2023; published 23 February 2023)

Investigations on epitaxial nanostructures with size of tens of nanometers have been a challenging issue for techniques that present high strain sensitivity but restricted spatial resolution. This is the case of recently developed x-ray nanoprobe techniques. Despite its inherent nondestructive character, submicron x-ray spots have only been successfully applied to the study of individual nanostructures which are either strain free or present extremely mild spatial lattice parameter gradients. Such limitation, with an uttermost barrier given by the diffraction limit, leads to voxel or pixel sizes between 5 and 10 nm obtained in coherent diffraction imaging or ptychographic reconstructions of real-space objects. Whenever the strain field of a nanostructure is successfully reconstructed from reciprocal space measurements, it cannot vary considerably in short distances since this would induce diffraction peak broadening and cause abrupt phase variations, leading to convergence issues on reconstruction algorithms. Here we show how epitaxial systems with large lattice mismatch and appreciable interfacial strain can be identified and directly analyzed throughout their strain field propagation in nanometer-thin crystalline membrane platforms, using the InGaAs/GaAs Stranski-Krastanov system as a model. The strain-induced footprint becomes observable along a few microns if the membrane thickness is comparable to the nanostructure size. It is possible to retrieve both interfacial strain and nanostructure size by probing individual objects.

DOI: [10.1103/PhysRevMaterials.7.026002](https://doi.org/10.1103/PhysRevMaterials.7.026002)

I. INTRODUCTION

In the last decade, semiconductor thin membranes have given rise to a promising field in nanotechnology and have attracted great attention of the scientific community [1–5]. The possibility to transfer a few nanometers thick membrane to a new support opened substantial potential applications in flexible electronics and optoelectronics [6,7]. Nanomembranes (NMs) based on semiconductor materials can host epitaxial quantum dots (QDs) that are of interest for the nanodevice industry [8–12]. Epitaxial QD systems such as InGaAs/GaAs or Ge/Si have reduced size (a few nanometers in height and tens of nanometers in radius) and large strain gradients, which can induce considerable modifications on the long-range strain fields in these NMs.

Semiconductor QDs have been investigated thoroughly in optoelectronic applications as single-electron transistors and single-photon light sources, with potential use in quantum computing. In the past decade, applications that go beyond simple confinement characteristics have emerged, allowing improvements in theoretical and experimental understanding

of quantum phenomena [13]. Entangled photon generation with a concurrence of high fidelity has been shown recently [14], while transistors working in the THz regime are feasible in the research scale [15]. In both cases, QDs represent a suitable system to investigate nonclassical properties. Particular interest in QDs on nanomembranes and thin layers explore the possibility of absorption/emission tuning via builtin or externally applied strain, which are able to bring distinct systems into resonance, fulfilling entanglement requirements for quantum computing [16,17].

Synchrotron radiation techniques have experienced a considerable evolution along the past decades [18–20]. The introduction of high-brilliance sources allowed the achievement of focused beams with sizes of a few hundreds of nanometers with coherence preservation [21,22]. Such probe is capable of illuminating single objects and, for the case of crystalline structures, can be used to retrieve real-space information with unprecedented resolution using scanning [23–25], full-field [26,27], or coherent imaging [28–31]. Nevertheless, some constraints to the broad use of the so-called phase-retrieval methods for coherent imaging remain. Besides the geometrical considerations usually described for diffraction limits [32–34], there is still a remarkable sample dependence for well succeeded experiments. In diffraction

*angeloms@fisica.ufmg.br

conditions, the objects must be homogeneous in composition and present mild lattice variations along their length, on the order of 1% maximum strain [35]. They also need to be relatively extended, with a typical size on the order of a hundred nanometers or more, in order to be suitable for image reconstruction due to pixel/voxel size limitations. Epitaxial objects with few nanometers and large strains are prohibitive to retrieval methods such as coherent diffraction imaging (CDI) or ptychography.

In this work we study InGaAs islands self-assembled on top of a 15-nm GaAs (001) nanomembrane (NM) as a model case and show how the strain induced or builtin highly mismatched systems on thin substrates can be extracted from spectroscopic results, since III-V semiconductors have well-known mechanical properties (see Ref. [16]). The layered system consists of an AlAs sacrificial layer grown on top of a GaAs buffer. AlAs is removed and allows the transfer of the NM to a Kapton foil (transparent to hard x rays) [3]. By carrying out nanofocused scanning x-ray diffraction (nano-XRD) measurements one can observe the large-range distortion of the NM caused by islands one order of magnitude smaller than the nanoprobe. Such an indirect marker allows the interpretation of the real-space strain map using finite element simulations. Regions subjected to homogeneous strain or strain gradients can also be quickly identified by locally mapping the Laplacian of the strain. The technique explored here can be extended to other epitaxial systems with small nanostructure size to unambiguously determine the interfacial strain.

II. EXPERIMENT

A lateral schematic view of the sample growth is shown in Fig. 1(a), with the relevant layer thickness depicted explicitly. The upper GaAs layer, together with the epitaxial $\text{In}_{0.5}\text{Ga}_{0.5}\text{As}$ islands (nominal growth concentration), were released from the original substrate and transferred to a new host support: a Kapton foil. The sample was grown by molecular-beam epitaxy (MBE) using a commercial machine (Karl Eberl MBE Komponenten, LNNano) on a GaAs (001) substrate. After an initial GaAs buffer, a nominal 40-nm AlAs sacrificial layer as well as the membrane structure (15-nm GaAs and InGaAs dots) were grown 10°C below the transition temperature of the c (4×4) and 4×2 reconstruction [36,37]. Transition from streak to spot-patterned diffraction, an indicator of transition from two-dimensional thin film growth to island formation [38], was monitored by reflection high-energy electron diffraction (RHEED), and occurred 1 min 40 s after the beginning of the growth. Such deposition time is nominally equivalent to a coverage of 2 monolayers (MLs). The dots were deposited with a nominal In and Ga rate of 0.02 ML/s. The growth conditions were expected to lead to the formation of an island ensemble with density of 1×10^9 islands/cm². The island density was extracted from a series of 20 atomic force microscopy (AFM) images taken on different regions of the grown wafer (2-in.) area. Each image had a $5 \times 5\text{-}\mu\text{m}^2$ area. Fluctuations of density observed in distinct regions did not surpass 20%. Finally, a similar QD density was also retrieved in released nanomembranes, where 15 AFM topographic images were carried out. The NM

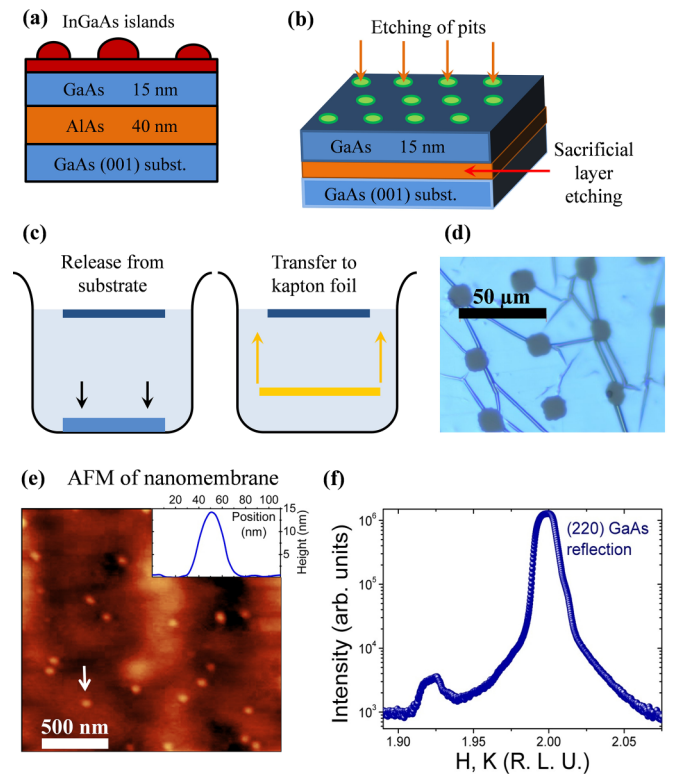


FIG. 1. (a) Sketch of the lateral view of the as-grown sample. (b),(c) Schematic representation of the release process of the NM. Etching holes on the sample allowed the access of the sacrificial layer, which was later removed, leading to the release of the ultra-thin GaAs layer with the islands. (d) Optical microscopic image of the NM after releasing. (e) AFM image of the released membrane sample, showing the islands' lateral sizes and density. Inset shows a topography profile of the island indicated with an arrow. (f) Longitudinal XRD scan of the NM in the vicinity of the 220 GaAs Bragg reflection.

transfer process is carried out using optical lithography as described in Ref. [3] and schematically represented in Figs. 1(b) and 1(c). Figure 1(d) shows an optical image of the NM after the releasing process, evidencing the etching spots and some membrane wrinkles, easily avoided in x-ray measurements due to their micrometer size.

The morphology and strain field of the NM on flat areas were studied by AFM and x-ray diffraction (XRD), respectively. A FlexAFM (Nanosurf) microscope was used in tapping mode. After the releasing process, the density retrieved by the AFM was found to be 0.8×10^9 islands/cm² as shown in Fig. 1(e). The average island size was retrieved as (25 ± 7) nm in radius and (15 ± 3) nm in height. With such density of objects, scanning nanofocused XRD measurements [39,40] are capable of illuminating a single island in some regions of the NM. Finite elements simulations (FEM) using a commercial software (COMSOL Multiphysics) were conducted in order to understand local inhomogeneities on the NM caused by the presence of the islands. For FEM calculations, we have used approximately 3×10^9 elements per simulation (depending on the membrane thickness and number of islands). The maximum element size was fixed at 1 μm

(lateral element size at membrane edges, far from islands), and the minimum element size was 4 nm (inside islands). Elastic parameters used for simulations were extracted from the COMSOL Multiphysics materials library (and verified at materials databases): (i) GaAs Poisson's ratio along the [100] direction: 0.31; Young's modulus along the [100] direction: 859 GPa; (ii) $\text{In}_{0.5}\text{Ga}_{0.5}\text{As}$: Poisson's ratio along the [100] direction: 0.33; Young's modulus along the [100] direction: 684 GPa.

XRD measurements were initially carried out using a millimeter-size beam, to probe the overall strain status of the NM and then with a nanofocused beam to verify local strain differences. Large-area measurements were performed in transmission geometry, mapping the vicinity of the 220 GaAs reflection, at the XRD2 beamline of the Brazilian Synchrotron Light Laboratory (LNLS), with the energy of the beam fixed to 10.2 keV ($l = 1.2155 \text{ \AA}$). In this setup a Pilatus 100-K detector was used to collect the diffraction data.

Diffraction maps of the NM, taken in the vicinity of the 220 GaAs reflection using the nanobeam of the ID01 beamline of the European Synchrotron Radiation Facility (ESRF), were used to verify the strain propagation around single islands. The nano-XRD experiment was carried out upon transmission geometry, at the ID01 beamline of the European Synchrotron Radiation Facility (ESRF), in Grenoble (France). The nanobeam was focused down to a $240 \times 430\text{-nm}^2$ (vertical \times horizontal) spot size using a set of Kirkpatrick-Baez (KB) mirrors. The energy of the beam was fixed at 8.388 keV (wavelength of 1.4781 \AA) during the nanodiffraction experiments, allowing an incident flux in the order of 10^{10} photons/second at the focused spot. The diffracted beam was recorded with a two-dimensional (2D) MAXIPIX photon-counting detector [41], with 516×516 pixels of 55 \mu m^2 pixel size, positioned 0.95 m from the sample. The sample was mounted on a fast xyz scanning piezoelectric stage, with a lateral stroke of 100 \mu m and a resolution of 2 nm. The piezo stage was itself mounted on a hexapod. In order to obtain strain-resolved maps, the nanobeam was scanned with the sample by making use of a piezo stage. The step size was fixed at 500 nm in each direction and the diffracted intensity was recorded for each real space position. Diffraction maps were acquired at different incidence angles around the Bragg condition, so the three-dimensional reciprocal space around the selected reflection could be reconstructed for each pixel in real space. By tracking the length and direction of the scattering vector \mathbf{Q} associated to the center of mass of each reconstruction, we could map strain and lattice tilt along selected areas of the NM. A sketch of the experimental setup is shown in Fig. 2(a).

III. RESULTS

A longitudinal/radial scan performed near the (220) GaAs reflection is shown in Fig. 1(f). An intense peak at the position corresponding to the bulk GaAs lattice parameter can be observed, while a weaker peak is retrieved centered at H , $K = 1.923$. The second peak may account for InGaAs islands. The 3.94% strain found by XRD is compatible with a ternary $\text{In}_{0.55}\text{Ga}_{0.45}\text{As}$ alloy, very close to the 3.85% expected for epitaxial $\text{In}_{0.5}\text{Ga}_{0.5}\text{As}$ islands on GaAs (the nominal 0.5:0.5

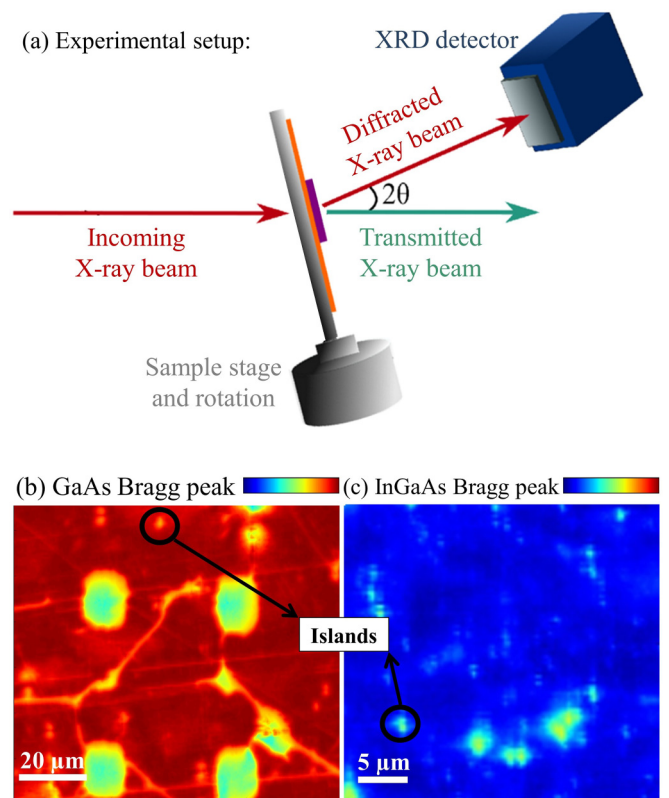


FIG. 2. (a) Schematic representation of the experimental setup used for nano-XRD measurements. (b) Intensity map of the NM at the GaAs peak, showing regions of flat, well aligned NM, as well as the etching holes (yellow circle-shaped regions). Orange regions might indicate the presence of islands (see for example the black circle). (c) Nano-XRD map at the NM (distinct region) near the InGaAs islands Bragg condition, confirming the presence, density and distribution of islands along the sample.

In:Ga composition was calculated from the growth rates of binary compounds in our system). Since the millimeter-sized beam illuminates an ensemble of 10^5 islands, this scan cannot be used to interpret local data.

By simultaneously combining high-speed continuous motion of the xyz scanning piezoelectric stage with high frequency MAXIPIX image recording and the nanofocused x-ray beam, space resolved diffraction maps could be retrieved for different incidence angles [42]. Nano-XRD measurements with the incident angle set at the 220 GaAs Bragg reflection led to intensity contrast at the etching pits as well as near islands and allowed the identification of different structures along the sample, as shown in Fig. 2(b). At the chosen color scale, dark red areas indicate regions with more diffraction counting, which are then associated with a flat, well aligned membrane, far from islands and with the lattice parameter close to the bulk GaAs value. The holes due to the etching process, which are a lack of membrane material, do not diffract, and are therefore easy to identify at such a condition. They appear as yellow circle-shaped regions following the mask pattern and their diameter is approximately 12 \mu m . Green lines can also be seen all along the map, and their existence is assigned to the presence of wrinkles and bends along the NM.

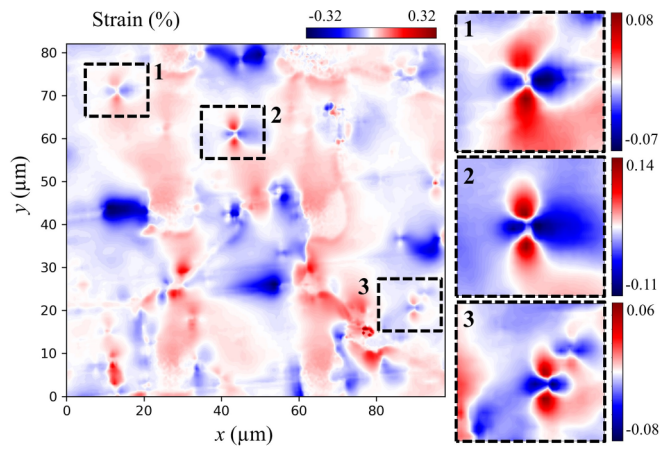


FIG. 3. In-plane strain map retrieved by nano-XRD for the sample surface in a region with reduced island density (measured around the 220 GaAs reflection). Three flowerlike features are highlighted in the map and depicted in detail in the lateral insets. Labels (1–3) are used to identify each feature. The color scale shows relative strain variation.

Finally, one can notice some orange dots spread throughout the image (see for example the region marked with a black circle), which are regions diffracting with a scattering vector \mathbf{Q} that does not correspond exactly to the expected bulk GaAs position, and must be associated with the InGaAs islands, since a larger lattice parameter is expected for them when compared to the flat GaAs membrane. A second nano-XRD map, with incident angle set at the expected islands' peak [$H = 1.923$, as shown in Fig. 1(f)], was also measured, in order to confirm and emphasize the information concerning the islands' presence, as one can see in Fig. 2(c). The lowest intensity blue regions now represent areas where the membrane exhibits a lattice parameter that does not match the InGaAs Bragg condition and can therefore be associated with flat NM or etching holes. Small dots, convoluted with the beam size, slightly smaller than $1 \mu\text{m}$ diameter, can be seen spreading all over the NM. Their existence can be attributed to isolated islands. One can notice, however, big and very intense features, which may represent well oriented clusters of islands.

Performing nano-XRD measurements at different incidence angles (θ) around the Bragg condition, one can reconstruct the three-dimensional reciprocal space associated to each real space position along the NM, mapping out strain along the scattering direction [25]. The result, processed in the form of a map, is shown in Fig. 3. This map shows that little in-plane strain variation along the (110) direction is observed along most of the NM surface, with a limited relative strain range between -0.32% and 0.32% , represented by the color scale. It is important to keep in mind that the membrane can present long range wrinkles and bent regions with tens of micrometers size, as shown in the Supplemental Material [43]. Given the size of these bent regions they should be noticed as a large area with the same color in the map, indicating that the bent angle induces a beam scattering at a distinct 2θ position due to a mild and smooth lattice misalignment. Such condition

is observed in large and color-constant blue (or red) regions along the map.

We focus our attention hereafter on features that show large strain gradients but are limited to reduced areas. In particular, flowerlike features were observed in different areas of the NM with the same strain pattern: an abrupt strain variation along distinct membrane directions, with the presence of lines of strain signal inversion (in white for our color scale) crossing each other at the center of the patterns. These lines are extended diagonally, separating petal-like regions of alternated compressive and tensile in-plane strain, probed at the (110) direction, and observed along both X and Y map directions. Since this experiment only observes strain in one direction (say, ε_{xx}), corresponding to the longitudinal scattering direction in reciprocal space, the perpendicular strain that remains at the membrane plane is perceived with the opposite signal since the objects have an in-plane circular symmetry. A negative (compressive) strain along ε_{xx} elastically induces a positive (tensile) strain in ε_{yy} . The observation of a center-symmetric strain field with a one-dimensional strain mapping procedure generates the flowerlike profile. Each of the observed features with the description above is marked in the map and depicted separately in the insets of Fig. 3. The density of flowerlike patterns in the map depicted in Fig. 3 is lower than the density of islands found by AFM in Fig. 1(e). It is important to notice that coherent and incoherent islands can coexist in the sample, but the second would not be perceived by XRD. On top of that, a coherent island will only be visible in Fig. 3 when it is strained and has a perfect lattice registry at the InGaAs/GaAs interface and the membrane is aligned both around the optical axis (diffracting on the x-ray detector) and in Bragg condition (rocking angle). This ensemble of selection conditions allows only a few islands to be captured by the strain mapping concomitantly. A more detailed explanation on why most of the islands are not visible by nano-XRD is included in the Supplemental Material [43].

The strain produced in these regions is compatible with the expected in-plane strain due to island/substrate interface. With a nm-thick semiconductor membrane it is expected that such a footprint of local lattice deformation becomes measurable for a submicron x-ray beam, even considering that an isolated island has a much smaller radius. In order to check that islands are present in the middle of flowerlike features we proceed plotting the Laplacian of the strain map. It is expected for a quasihomogeneous strain that the Laplacian behaves showing smooth variations and reduced values ($\nabla^2\varepsilon \cong 0$). If a strong strain gradient is causing the observed feature, large values of the Laplacian must be found ($\nabla^2\varepsilon > 0$), preserving a similar symmetry with respect to the object observed in the strain map [44]. Moreover, the Laplacian allows us to locate both isolated islands, as well as island clusters or strong strain gradient objects sitting on top of bent nanomembrane regions.

The strain conditions that lead to a nonzero Laplacian of the measured data are schematically depicted in Fig. 4(a). For objects showing strain gradient it is expected that both local strain (ε) and strain Laplacian ($\nabla^2\varepsilon$) are different from zero. This is the case for regions ranging from copper to yellow light colors in the main map of Fig. 4(b). One observes that bent regions of the NM are also highlighted in this map. The fourfold symmetry of the objects selected in the insets of

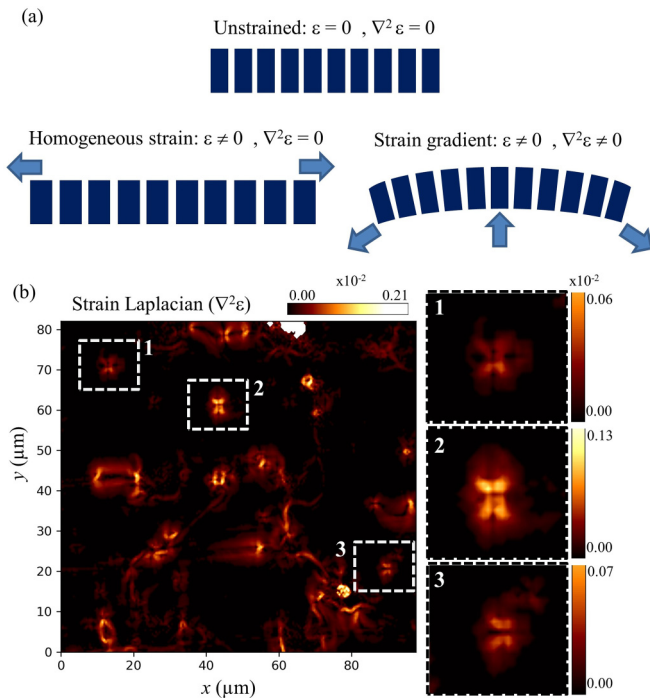


FIG. 4. (a) Representation of membranes (slabs) of materials subjected to zero strain, a homogeneous strain along one in-plane axis and a strain gradient caused by bending. The conditions that allow for identification of each strain type using strain and strain Laplacian maps are represented in the figure. (b) Map of the strain Laplacian extracted from the data of Fig. 3. Regions of inhomogeneous strain ascribed to the presence of isolated islands in Fig. 3 are highlighted in the insets.

Fig. 3 are again observed here with a distinct orientation since most of the gradient is found to be maximum between the petal-like regions of these objects (see insets).

Finite element method (FEM) simulations with single and multiple islands sitting on top of membranes with $10 \times 10 \text{ mm}^2$ and $20 \times 20 \text{ mm}^2$ lateral size were carried out in order to explore the strain profile shape and strain decaying. Variables such as membrane thickness (10–30 nm, 5-nm steps), island size (15–35 nm radius, with 5-nm steps), and interfacial strain (0.1%, 0.2%, and 0.5–10%, in 0.5% steps) were explored along the ranges indicated in brackets. Figure 5(a) shows the view of a cut in the middle of a 15-nm-thin membrane with five islands on top (nominal membrane is thinner and difference is much bigger than expected growth error). In this simulation, islands have a distinct interfacial strain, ranging 2–5% (see figure caption for specifications) and are separated by distances compatible with the experimental island density. One clearly observes flowerlike shapes in which strained islands lie in each flower center.

Selected simulated cuts extracted from island strain profiles varying the interfacial strain are shown in Fig. 5(b) for a fixed membrane thickness of 15 nm. One observes that large island-membrane interfacial strain conditions lead to extended and pronounced effects on the membrane lattice, which are above the detection threshold for the present experiment. For built-in interfacial strain conditions above 1% (red curve) the footprint of the presence of a single island is easily detectable,

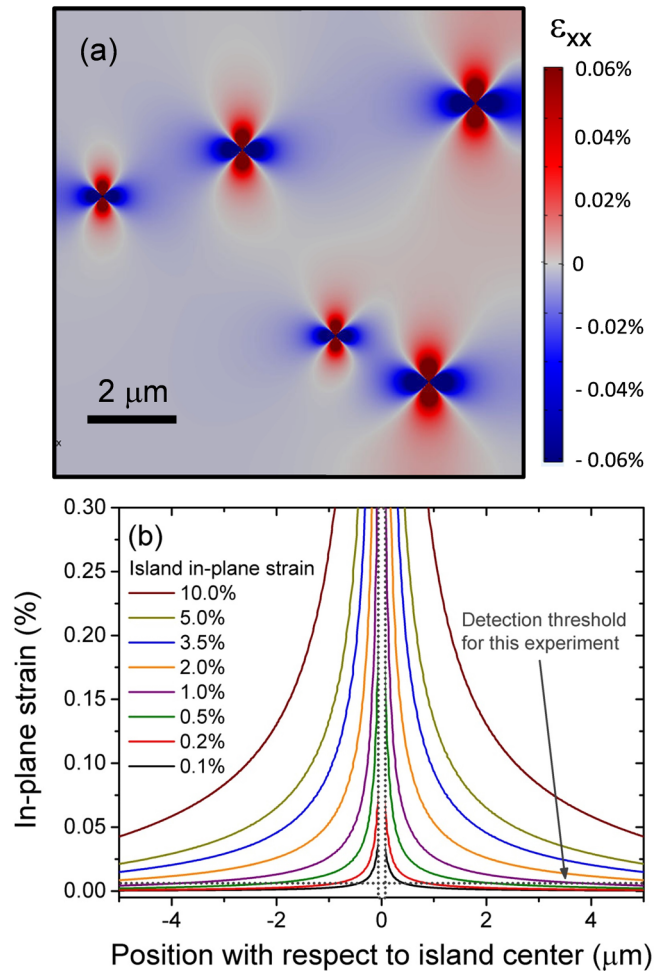


FIG. 5. (a) Finite element simulation of the in-plane strain ϵ_{xx} inside a 15-nm-thin GaAs membrane containing five $\text{In}_{0.5}\text{Ga}_{0.5}\text{As}$ islands. The two rightmost islands have 5% in-plane strain, the top-middle island has 3.5% in-plane strain, and the smaller flowers (leftmost) are generated by islands with 2% strain. Island radius was fixed to 25 nm. The membrane surface has $10 \times 10 \text{ mm}^2$ and the extracted profile is located in the middle of the membrane thickness. (b) Strain profiles for distinct interfacial conditions using a FEM simulated isolated island with 25-nm radius atop a 15-nm-thick GaAs membrane. Detection threshold for the experimental setup used in this paper is represented by a horizontal dotted line.

straining an area with lateral width larger than 400 nm. It is therefore likely that extended strain profiles as those shown in Fig. 3 allow for recognition of the interfacial condition of nano-objects generating them.

A quantitative exploration of the strain at the interface of a single island is carried out crossing the experimental data of islands 1–3 depicted in Fig. 3. In order to achieve such a condition, FEM simulations must reproduce the measured strain decay. Profiles extracted from FEM simulations of isolated (single) islands in a $20 \times 20\text{-mm}^2$ membrane are shown in Fig. 6, capturing the in-plane strain decay along the nanomembrane due to the influence of single island. Solid dots represent the average strain measured by nano-XRD at spots along one axis of each flowerlike profile for the three islands highlighted in Figs. 3 and 4. One can notice that in all cases the mono-

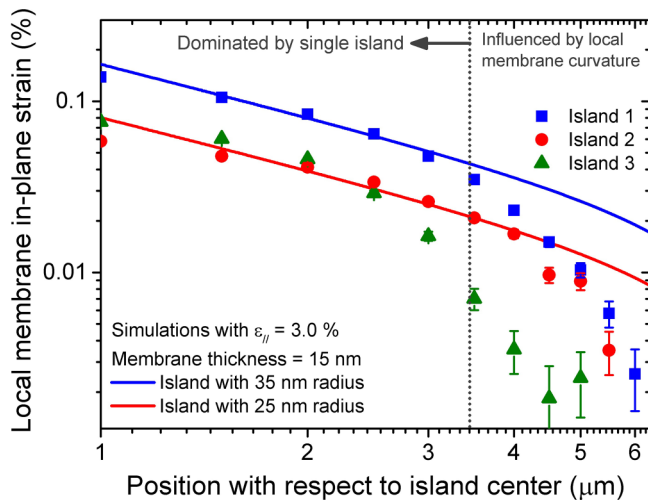


FIG. 6. Experimental strain profiles (dots) and finite element simulations (solid lines) with respect to the island center position for the islands depicted in Figs. 3 and 4. For both simulated profiles the island interfacial strain was fixed to 3.0% with a membrane thickness of 15 nm. The strain profile for island 1 is fitted using a 35-nm-radius lens-shaped nanostructure, while results for islands 2 and 3 are fitted with the simulated profile from a 25-nm-radius nanostructure.

tonic decrease of strain exhibits a smooth decay up to 3.5 μm away from the island center position, followed by more abrupt strain changes that take place after such threshold. We ascribe this difference in strain behavior to an influence of the local bowing of the membrane in regions far from the island concentrated strain gradient, as shown in the Supplemental Material [43]. The strain behavior in the vicinity of islands 2 and 3 present a behavior compatible with coherently strained lens-shaped objects with (25 ± 3) nm radii sitting atop of a 15-nm-thin membrane. The reduced membrane thickness with respect to the nominal GaAs layer nominal thickness was observed in NMs and rolled up tubes subjected to XRD measurements, due to the presence of a thin surface oxidation layer on both interfaces. Island 1 is better fitted with a curve corresponding to a simulated structure with (35 ± 3) nm radius also sitting on a 15-nm membrane. The strain for all simulations was fixed to $(3.0 \pm 0.2)\%$. Error bars were estimated by changes in the simulated island size and comparison of extracted profiles with experimental strain curves within regions with strain decay dominated by single islands.

IV. CONCLUSION

In this work, we have shown how to overcome the probe size limitation on nano-XRD measurements and retrieve the strain of nanostructures one order of magnitude smaller than

the x-ray beam size. Using a beam with hundreds of nanometers we extracted experimental Laplacian of strain gradient maps, which were in turn able to provide the location of $\text{In}_{0.5}\text{Ga}_{0.5}\text{As}$ islands and bent membrane regions without ambiguity. Interfacial strain of objects deforming the membrane were retrieved by FEM simulations and fitted to experimental profiles. The geometrical limitation of the experiment (detection of 0.01% strain) is sufficient for mapping distortions in strained structures where a direct imaging of the strain field is not directly possible using synchrotron imaging techniques or electron microscopy (e.g., geometric phase analysis in transmission electron microscopy). The discussed methodology exhibits all its potential when applied to highly strained nanostructures (more than 1% strain) supported in single-crystalline layers with strong lattice registry as exhibited in epitaxial growth conditions.

There is a potential impact of direct observing the strain field decay near quantum dots systems. QDs have been targeted very recently due to their potential of generating entangled photons on demand and meeting the stringent requirements of the quantum repeater schemes [45]. By extremely reducing low multiphoton emission probability [46], and providing photon indistinguishability and wavelength tunability [47] they became an affordable choice for testing quantum computing devices. Since the construction of such devices lies on the combination of low-density or isolated nanostructures with lithographic processes that usually thin down the QDs environment in one or more directions, such as in micropillars [48], the full control of the surrounding strain field adds another degree of freedom for tailoring transition states from the μeV to the meV range. Such strain-driven tuning hinders the exploration of nondestructive strain imaging techniques, such as the one discussed here, mandatory in order to achieve high fidelity capabilities.

ACKNOWLEDGMENTS

The authors acknowledge FAPESP, FAPEMIG, CAPES, and CNPq for financial support. Beamtime was granted at the XRD2 beamline by the LNLS/MCTI (Proposal No. 20170126) and at the ID01 beamline by ESRF (Proposal No. MA-3581). We acknowledge access to the MBE of the LNNano.

Y.B., L.A.B.M., and A.M. planned the research and wrote the manuscript. Sample synthesis and preparation were performed by B.L.T.R., A.G.Jr., and Ch.D. Synchrotron experiment was performed by L.A.B.M., M-I.R., and T.U.S. Data analysis was carried out by Y.B., L.A.B.M., and A.M. All authors discussed the data and contributed to the manuscript.

The authors declare no competing financial interest.

- [1] W. Peng, Z. Aksamija, S. A. Scott, J. J. Endres, D. E. Savage, I. Knezevic, M. A. Eriksson, and M. G. Lagally, *Nat. Commun.* **4**, 1339 (2013).
 [2] M. A. Yoder, Z. Yan, M. Han, J. A. Rogers, and R. G. Nuzzo, *J. Am. Chem. Soc.* **140**, 9001 (2018).

- [3] A. Malachias, Y. Mei, R. K. Annabattula, Ch. Deneke, P. R. Onck, and O. G. Schmidt, *ACS Nano* **2**, 1715 (2008).
 [4] K. Sim, Z. Rao, Z. Zou, F. Ershad, J. Lei, A. Thukral, J. Chen, Q. Huang, J. Xiao, and C. Yu, *Sci. Adv.* **5**, eaav9653 (2019).

- [5] T-H. Chang, K. Xiong, S. H. Park, G. Yuan, Z. Ma, and J. Han, *Sci. Rep.* **7**, 6360 (2017).
- [6] A. H. MacDonald, P. Schiffer, and N. Samarth, *Nat. Mater.* **4**, 195 (2005).
- [7] J. Novák, I. Vávra, Z. Križanová, S. Hasenöhrl, J. Šoltýs, M. Reiffers, and P. Štrichovanec, *Appl. Surf. Sci.* **256**, 5672 (2010).
- [8] Ch. Deneke, A. Malachias, A. Rastelli, L. Mercedes, M. Huang, F. Cavallo, O. G. Schmidt, and M. G. Lagally, *ACS Nano* **6**, 10287 (2012).
- [9] A. J. Garcia Jr., L. N. Rodrigues, S. F. Covre da Silva, S. L. Morelhão, O. D. D. Couto, Jr., F. Iikawa, and Ch. Deneke, *Nanoscale* **11**, 3748 (2019).
- [10] M. Kroutvar, Y. Ducommun, D. Heiss, M. Bichler, D. Schuh, G. Abstreiter, and J. J. Finley, *Nature (London)* **432**, 81 (2004).
- [11] B. Ellis, M. A. Mayer, G. Shambat, T. Sarmiento, J. Harris, E. E. Haller, and J. Vučković, *Nat. Photonics* **5**, 297 (2011).
- [12] Y. R. Wang, I. S. Han, C-Y. Jin, and M. Hopkinson, *ACS Appl. Nano Mater.* **3**, 4739 (2020).
- [13] T. Kipp, H. Welsch, Ch. Strelow, Ch. Heyn, and D. Heitmann, *Phys. Rev. Lett.* **96**, 077403 (2006).
- [14] K. D. Zeuner, K. D. Jöns, L. Schweickert, C. R. Hedlund, C. N. Lobato, T. Lettner, K. Wang, S. Gyger, E. Schöll, S. Steinhauer, M. Hammar, and V. Zwiller, *ACS Photonics* **8**, 2337 (2021).
- [15] M. Asgari, D. Coquillat, G. Menichetti, V. Zannier, N. Diakonova, W. Knap, L. Sorba, L. Viti, and M. S. Vitiello, *Nano Lett.* **21**, 8587 (2021).
- [16] S. Mendach, S. Kiravittaya, A. Rastelli, M. Benyoucef, R. Songmuang, and O. G. Schmidt, *Phys. Rev. B* **78**, 035317 (2008).
- [17] T. Lettner, S. Gyger, K. D. Zeuner, L. Schweickert, S. Steinhauer, C. R. Hedlund, S. Stroj, A. Rastelli, M. Hammar, R. Trotta, K. D. Jöns, and V. Zwiller, *Nano Lett.* **21**, 10501 (2021).
- [18] M. A. Pfeifer, G. J. Williams, I. A. Vartanyants, R. Harder, and I. K. Robinson, *Nature (London)* **442**, 63 (2006).
- [19] M. C. Newton, S. J. Leake, R. Harder, and I. K. Robinson, *Nat. Mater.* **9**, 120 (2010).
- [20] F. Meirer and B. M. Weckhuysen, *Nat. Rev. Mater.* **3**, 324 (2018).
- [21] S. J. Leake, G. A. Chahine, H. Djazouli, T. Zhou, C. Richter, J. Hilhorst, L. Petit, M-I. Richard, C. Morawe, R. Barrett, L. Zhang, R. A. Homs-Regojo, V. Favre-Nicolin, P. Boesecke, and T. U. Schulli, *J. Synchrotron Radiat.* **26**, 571 (2019).
- [22] A. Bjorling, S. Kalbfleisch, M. Kahnt, S. Sala, K. Parfeniukas, U. Vogt, G. Carbone, and U. Johansson, *Opt. Express* **28**, 5069 (2020).
- [23] G. A. Chahine, M-I. Richard, R. A. Homs-Regojo, T. N. Tran-Caliste, D. Carbone, V. L. R. Jacques, R. Grifone, P. Boesecke, J. Katzer, I. Costina, H. Djazouli, T. Schroeder, and T. U. Schulli, *J. Appl. Crystallogr.* **47**, 762 (2014).
- [24] C. Kim, V. Chamard, J. Hallmann, T. Roth, W. Lu, U. Boesenberg, A. Zozulya, S. Leake, and A. Madsen, *Phys. Rev. Lett.* **121**, 256101 (2018).
- [25] L. A. B. Marçal, E. Oksenberg, D. Dzhigaev, S. Hammarberg, A. Rothman, A. Bjorling, E. Unger, A. Mikkelsen, E. Joselevich, and J. Wallentin, *ACS Nano* **14**, 15973 (2020).
- [26] J. Hilhorst, F. Marschall, T. N. Tran Thi, A. Last, and T. U. Schulli, *J. Appl. Crystallogr.* **47**, 1882 (2014).
- [27] L. A. B. Marçal, D. Dzhigaev, Z. Zhang, E. Sanders, A. Rothman, E. Zatterin, E. Bellec, T. U. Schulli, A. Mikkelsen, E. Joselevich, and J. Wallentin, *Phys. Rev. Mater.* **6**, 054408 (2022).
- [28] V. Favre-Nicolin, F. Mastropietro, J. Eymery, D. Camacho, Y. M. Niquet, B. M. Borg, M. E. Messing, L-E. Wernersson, R. E. Algra, E. P. A. M. Bakkers, T. H. Metzger, R. Harder, and I. K. Robinson, *New J. Phys.* **12**, 035013 (2010).
- [29] A. Björling, L. A. B. Marçal, J. Solla-Gullon, J. Wallentin, D. Carbone, and F. R. N. C. Maia, *Phys. Rev. Lett.* **125**, 246101 (2020).
- [30] D. Dzhigaev, Z. Zhang, L. A. B. Marçal, S. Sala, A. Björling, A. Mikkelsen, and J. Wallentin, *New J. Phys.* **23**, 063035 (2021).
- [31] D. Dzhigaev, Y. Smirnov, P-A. Repecaud, L. A. B. Marçal, G. Fevola, D. Sheyfer, Q. Jeangros, W. Cha, R. Harder, A. Mikkelsen, J. Wallentin, M. Morales-Masis, and M. E. Stuckelberger, *Commun. Mater.* **3**, 38 (2022).
- [32] I. Robinson and R. Harder, *Nat. Mater.* **8**, 291 (2009).
- [33] A. F. Pedersen, V. Chamard, and H. F. Poulsen, *Opt. Express* **26**, 23411 (2018).
- [34] R. A. Vicente, I. T. Neckel, S. K. R. S. Sankaranarayanan, J. Solla-Gullon, and P. S. Fernandez, *ACS Nano* **15**, 6129 (2021).
- [35] Z. Wang, O. Gorobtsov, and A. Singer, *New J. Phys.* **22**, 013021 (2020).
- [36] S. F. C. da Silva, E. M. Lanzoni, V. A. Barboza, A. Malachias, S. Kiravittaya, and Ch. Deneke, *Nanotechnology* **25**, 455603 (2014).
- [37] S. F. C. da Silva, E. M. Lanzoni, A. Malachias, and Ch. Deneke, *J. Cryst. Growth* **425**, 39 (2015).
- [38] J. Kwoen and Y. Arakawa, *Cryst. Growth Des.* **20**, 5289 (2020).
- [39] L. A. B. Marçal, M-I. Richard, R. Magalhães-Paniago, F. Cavallo, M. G. Lagally, O. G. Schmidt, T. U. Schulli, Ch. Deneke, and A. Malachias, *Appl. Phys. Lett.* **106**, 151905 (2015).
- [40] L. A. B. Marçal, S. Benter, A. Irish, D. Dzhigaev, E. Oksenberg, A. Rothman, E. Sanders, S. Hammarberg, Z. Zhang, S. Sala, A. Björling, E. Unger, A. Mikkelsen, E. Joselevich, R. Timm, and J. Wallentin, *Phys. Rev. Mater.* **5**, L063001 (2021).
- [41] C. Ponchut, J. M. Rigal, J. Clement, E. Papillon, A. Homs, and S. Petitdemange, *J. Instrum.* **6**, C01069 (2011).
- [42] C. Mocuta, J. Stangl, K. Mundboth, T. H. Metzger, G. Bauer, I. A. Vartanyants, M. Schmidbauer, and T. Boeck, *Phys. Rev. B* **77**, 245425 (2008).
- [43] See Supplemental Material at <http://link.aps.org/supplemental/10.1103/PhysRevMaterials.7.026002> for reciprocal spacing mappings of individual islands along the nanomembrane.
- [44] V. Harbola, S. Crossley, S. S. Hong, D. Lu, Y. A. Birkhölzer, Y. Hikita, and H. Y. Hwang, *Nano Lett.* **21**, 2470 (2021).
- [45] J. Neuwirth, F. B. Basset, M. B. Rota, E. Roccia, C. Schimpf, K. D. Jöns, A. Rastelli, and R. Trotta, *Mater. Quantum Technol.* **1**, 043001(2021).
- [46] X. Huang, J. Yang, C. Song, M. Rao, Y. Yu, and S. Yu, *Nanophotonics* **11**, 3093 (2022).
- [47] C. Schimpf, M. Reindl, F. Basso Basset, K. D. Jons, R. Trotta, and A. Rastelli, *Appl. Phys. Lett.* **118**, 100502 (2021).
- [48] L. Gines, M. Moczala-Dusanowska, D. Dlaka, R. Hořák, J. R. Gonzales-Ureta, J. Lee, M. Ježek, E. Harbord, R. Oulton, S. Höfling, A. B. Young, C. Schneider, and A. Predojević, *Phys. Rev. Lett* **129**, 033601 (2022).